



Pagano, Arianna Gea and Magnanimo, Vanessa and Weinhart, Thomas and Tarantino, Alessandro (2019) Exploring the micromechanics of non-active clays via virtual DEM experiments. Geotechnique. ISSN 0016-8505 , <http://dx.doi.org/10.1680/jgeot.18.p.060>

This version is available at <https://strathprints.strath.ac.uk/67196/>

Strathprints is designed to allow users to access the research output of the University of Strathclyde. Unless otherwise explicitly stated on the manuscript, Copyright © and Moral Rights for the papers on this site are retained by the individual authors and/or other copyright owners. Please check the manuscript for details of any other licences that may have been applied. You may not engage in further distribution of the material for any profitmaking activities or any commercial gain. You may freely distribute both the url (<https://strathprints.strath.ac.uk/>) and the content of this paper for research or private study, educational, or not-for-profit purposes without prior permission or charge.

Any correspondence concerning this service should be sent to the Strathprints administrator: strathprints@strath.ac.uk

Exploring the micromechanics of non-active clays via virtual DEM experiments

Arianna Gea Pagano*, Vanessa Magnanimo**, Thomas Weinhart** and Alessandro
Tarantino*

AFFILIATION:

* Department of Civil and Environmental Engineering, University of Strathclyde

** Multiscale Mechanics Group, University of Twente

ABSTRACT

The micromechanical behaviour of clays cannot be investigated experimentally in a direct fashion due to the small size of clay particles. An insight into clay mechanical behaviour at the particle scale can be gained via virtual experiments based on the Discrete Element Method (DEM). So far, most DEM models for clays have been designed on the basis of theoretical formulations of inter-particle interactions, with limited experimental evidence of their actual control over the clay's macroscopic response. This paper presents a simplified two-dimensional DEM framework where contact laws were inferred from indirect experimental evidence at the microscale by Pedrotti and Tarantino, 2017 (particle-to-particle interactions were probed experimentally by varying the pore-fluid chemistry, and the resulting effect explored via Scanning Electron Microscopy and Mercury Intrusion Porosimetry). The proposed contact laws were successfully tested against their ability to reproduce qualitatively the compression behaviour of clay with pore-fluids of varying pH and dielectric permittivity. The DEM framework presented in this work was intentionally kept simple in order to demonstrate the robustness of the micromechanical concept underlying the proposed contact laws. It is anticipated that a satisfactory quantitative prediction would be achieved by

moving to a three-dimensional formulation, by considering polydisperse specimens, and by refining the contact laws.

1. INTRODUCTION

The macroscopic response of geomaterials is controlled by the processes occurring at the microscale. Understanding these processes is therefore the key to interpret experimental data, and to inform 'continuum' macroscopic constitutive models.

For the case of granular materials, microscale processes have been investigated experimentally in terms of the interparticle forces (Cavarretta, et al., 2010) and particle kinematics (Andò, et al., 2012a; Andò, et al., 2012b). The microscopic mechanisms observed experimentally have been translated into DEM (Discrete Element Method) models, which have been used as a virtual laboratory to investigate fundamental aspects of the macroscopic behaviour of soil (O' Sullivan, et al., 2006), including strain localisation (Kawamoto, et al., 2018; Iwashita & Oda, 1997), induced anisotropy (Guo & Zhao, 2012), soil crushing and aggregate deformability (Thornton, et al., 1996; Cheng, et al., 2003; Bolton, et al., 2008; Ueda et al., 2013; Asadi et al., 2018), wave propagation and small strain stiffness (Magnanimo et al., 2008; Mouraille, 2009; O'Donovan et al., 2012).

On the other hand, microscale processes in clays cannot be easily investigated in a direct fashion due to the small size of clay particles. In addition, inter-particle forces in clays may be both electro-chemical and mechanical, in contrast to granular materials where only mechanical inter-particle forces are significant. Due to the lack of direct observations of such interactions, the formulation of a micromechanical model is not straightforward.

Several approaches have been proposed in the literature to derive micromechanical models for clays. Anandarajah and his co-authors (Anandarajah, 2000; Yao & Anandarajah, 2003, Anandarajah & Amarasinghe, 2012) presented a DEM micromechanical model based on the assumption that inter-particles forces are associated with double-layer repulsion and van der Waals attraction. Ebrahimi et al. (2014) and Ebrahimi et al. (2016) derived the interaction between clay platelets from full atomistic Molecular Dynamics (MD) simulations of the clay-water system, and used this information to develop a multiscale methodology for modelling the formation of clay aggregates. Sjoblom (2015) also included van der Waals attractive forces, Stern repulsion, Born repulsion, and edge-to-face and edge-to-edge attractive forces, again via MD simulations.

Although these contributions are based on advanced numerical tools, the underlying micromechanical models have been built on a theoretical basis. Except for Ebrahimi et al., unknown parameters at the microscale have been calibrated to fit specific macroscopic experimental responses, whereas direct experimental observations at the microscale for the calibration and validation of the proposed models are absent. Given the difficulty to achieve direct microscale evidence, an 'indirect' approach can support further understanding. In particular, a step forward in the investigation of the microscale mechanisms in clays would consist of selecting possible inter-particle interactions on the basis of 'indirect' experimental evidence at the microscale (e.g. Scanning Electron Microscope, Mercury Intrusion Porosimetry), translating them into a DEM framework, and validating the response of the discrete assembly against macroscopic clay behaviour in various conditions.

This paper presents the DEM validation of a conceptual micromechanical model able to describe the microscale mechanisms governing the one-dimensional compression of non-active clays. The micromechanical model was developed in a separate study by Pedrotti and Tarantino (2017), who

investigated experimentally the effect of the pore-fluid chemistry of kaolin clay specimens on the particle-to-particle interactions using a combination of Mercury Intrusion Porosimetry (MIP) and Scanning Electron Microscope imaging (SEM). The micromechanical model inferred from this 'indirect' microscale experimental evidence was used in this study to design the constitutive contact laws of a simplified two-dimensional DEM framework, using the open source C++ code MercuryDPM (Weinhart et al. 2016; Weinhart et al. 2017; source: <http://www.mercurydpm.org/>). Clay platelets were modelled as rod-shaped particles made of spherical elementary units, designed to behave as single elements. Virtual clay specimens were created by considering monodisperse assemblies of rods. Piece-wise linear contact laws including attractive and repulsive long-range interactions were designed in order to simulate the positive/negative charge characterising the clay particle surface.

The contact laws were tested against the ability of the DEM framework to reproduce qualitatively some aspects of the one-dimensional compression behaviour of clay observed experimentally and, hence, corroborate the underlying micromechanical concept. These include the effect of pH and dielectric permittivity of the pore-fluid on the virgin loading and unloading-reloading lines, and the dependency of the slope of the unloading-reloading lines on the pre-consolidation stress. Despite the simplicity of the proposed model (2D environment, monodisperse specimens, linear contact laws), distinct microscale mechanisms could be effectively linked with clay response at the macroscale. The micromechanical model validated in this paper therefore aims at laying the ground for more advanced DEM analyses.

2. BACKGROUND: CONCEPTUAL MICROMECHANICAL MODEL FOR NON-ACTIVE CLAYS

Pedrotti and Tarantino (2017) formulated a conceptual micromechanical model describing the mechanisms underlying reversible and non-reversible compression of non-active clays. The conceptual model was based on the results of an extensive experimental investigation into the microscopic and macroscopic behaviour of kaolinite, including MIP, SEM imaging, and oedometer tests.

The model was based upon the assumption that both mechanical and electro-chemical forces affect inter-particle interactions. Coulombian forces, due to the presence of permanent charges on the surface of clay particles, were assumed to be the only electro-chemical forces controlling the interaction between clay particles. Particle faces were assumed to be negatively charged due to isomorphic substitution of cations with negative charges, whereas particle edges were assumed to be either negatively or positively charged depending on whether the pH is alkaline or acidic respectively. A schematic representation of the microscopic mechanisms inferred by Pedrotti and Tarantino is shown in Figure 1.

For an alkaline pore-fluid, the negative charge of both particle faces and edges generates a repulsive Coulombian force, preventing particles from creating a contact and resulting in a sub-parallel 'face-to-face' (FF) configuration. In this case, an increase or decrease of external load was assumed to generate only reversible volume change (mechanism 'i' in Figure 1).

For an acidic pore-fluid, the positive charge of the particle edges and the negative charge of the particle faces were assumed to generate an attractive Coulombian force, resulting in the creation of 'edge-to-face' (EF) contacts between particles. This type of contact was assumed to cause both reversible and non-reversible micro-mechanisms. Reversible mechanisms refer to the case when

particles in contact, subjected to loading or unloading, tilt with respect to each other with no contact disengagement (mechanism 'ii' in Figure 1). On the other hand, non-reversible volume change was attributed to the loss of edge-to-face contacts (i.e. slippage or normal detachment) due to external loading (mechanism 'iii' in Figure 1). After the non-reversible loss of a contact, particles were assumed to dispose in a sub-parallel 'face-to-face' configuration and, hence, give rise to reversible mechanisms.

Finally, for both edge-to-face and face-to-face configurations, the magnitude of the repulsive Coulombian interaction controlling the distance between particles during loading/unloading reversible paths was assumed to be controlled by the relative dielectric permittivity of the pore-fluid, ε (intended as the relative permittivity, i.e. the ratio between the absolute permittivity and the permittivity of the vacuum). This dependency may be shown, for instance, by considering the repulsive Coulombian force developing between two facing circular plates (Pedrotti & Tarantino, 2017):

$$F = \frac{\pi a^2}{8\varepsilon_0\varepsilon} \rho^2 \left(\frac{z}{\sqrt{a^2 + z^2}} - 1 \right)$$

1

where a is the radius of the plates, z is the plate distance, ρ is the electrical charge distribution on the plates, and ε_0 is the permittivity of the vacuum. According to Equation 1, small values of the dielectric permittivity of the pore-fluid (e.g. air) give rise to high repulsive/attractive interactions, and vice-versa.

3. DISCRETE ELEMENT METHOD FRAMEWORK

In this work, the Discrete Element Method (Cundall & Strack, 1979) was used to simulate the behaviour of a non-active clay subjected to 1-D loading and unloading. DEM analyses describe the particle-to-particle interactions occurring within particle aggregates. The basic input of a DEM

model are the contact forces and torques acting on each particle due to the interactions with other particles and with the domain boundaries. Once the forces and torques are known, the dynamic motion of the particles is determined by integrating Newton’s equations of motion for the translational and rotational degrees of freedom.

The simplest contact model describing the normal mechanical interaction between pairs of spherical particles, f_{ij}^n , involves a linear-elastic repulsive force (particles repel each other with no energy loss) and a linear dissipative force (acting against the relative velocity and resulting in a loss of energy), as in Luding (2008):

$$f_{ij}^n = \begin{cases} 0, & \delta_{ij}^n \leq 0 \\ k_n \delta_{ij}^n + \gamma_n v_{ij}^n, & \delta_{ij}^n > 0 \end{cases} \quad 2$$

where δ_{ij}^n and v_{ij}^n are the normal overlap and the normal relative velocity between spheres i and j respectively (taken on the line connecting the centres of the spheres), k_n is the normal stiffness at the contact, and γ_n is the damping coefficient. A non-zero tangential interaction f_{ij}^t can also be considered, arising when spheres in contact ($\delta_{ij}^n > 0$) experience a relative displacement in the tangential direction:

$$f_{ij}^t = \begin{cases} 0, & \delta_{ij}^n \leq 0 \\ k_t \delta_{ij}^t + \gamma_t v_{ij}^t, & \delta_{ij}^n > 0 \\ \mu f_{ij}^n, & |k_t \delta_{ij}^t| > \mu f_{ij}^n \end{cases} \quad 3$$

where k_t is the tangential stiffness at the contact, δ_{ij}^t and v_{ij}^t are the relative tangential displacement and the relative tangential velocity respectively, γ_t is the tangential damping coefficient, and μ is the friction coefficient. The tangential contact model can be extended to the rotational degree of freedom by introducing a rolling resistance f_{ij}^{ro} , calculated by substituting the

terms δ_{ij}^t , k_t , v_{ij}^t and γ_t in Equation 3 with the relative rotation δ_{ij}^{ro} , the rolling stiffness k_{ro} , the rolling velocity v_{ij}^{ro} and the rolling damping coefficient γ_{ro} respectively.

Starting from the basic interactions described in Equation 2 and 3, two specific aspects of clay DEM modelling were addressed in this study: a) the creation of elongated particles, and b) the introduction of additional inter-particle interactions to simulate the effect of the positive/negative charge carried by clay particles.

3.1. 2D Modelling of clay particles

Kaolin clay particles naturally occur as small hexagonal-shaped elements, with particle sizes usually falling in the range 0.1 – 10 μm . Particles are typically elongated, and the ratio between the thickness of a particle and its main dimension is usually around 1/10 (Mitchell & Soga, 2005). In 2D analyses, kaolin particles can therefore be schematised as rod-like elements, having a 1-to-10 ratio between thickness and length.

In this study, spheres were used to create rod-like particles constrained to move in a plane. Each sphere represents an elementary DEM unit, i.e. initial information such as dimensions and density were assigned individually to each sphere, as well as the contact law parameters. However, an additional attractive force was introduced to 'bond' together groups of spheres into single rods:

$$f_{bond} = k_n \delta_{bond} \quad 4$$

where f_{bond} is the attractive force bonding together spheres in the same rod, k_n is the normal stiffness at the contact (as for Equation 2), and δ_{bond} is the overlap between spheres belonging to the same rod (input parameter). Therefore, although each sphere was treated separately as an elementary unit, each group of spheres forming a rod behaved as a single elongated particle,

(similarly to crushable particles or deformable agglomerates modelled by Thornton, et al. 1996, Cheng, et al. 2003, Bolton, et al. 2008, Ueda et al. 2013, Asadi et al., 2018).

For the sake of simplicity, equal rods of 19 spheres were considered in this study (Figure 2). The overlap δ_{bond} was taken as being equal to the radius of each sphere, in order to obtain a thickness-to-length ratio for each rod equal to 1/10. The properties of the elementary spheres used in this work are given in Table 1. The assigned properties yielded a constant collision time $t_c = 2.6\text{e-}9$ s and a restitution coefficient equal to 0.9. A constant time step taken as $\Delta t = 0.02t_c$ could therefore be used. It is worth noticing that particle properties (e.g. stiffness, mass, inertia) have been selected so that the simulation results may be qualitatively representative of the real problem, despite the 2D simplification of the simulated specimens. Furthermore, preliminary simulations on slightly polydisperse specimens showed an overall compression behaviour qualitatively comparable with that of monodisperse assemblies. Monodisperse specimens were therefore adopted here in order to save computation time without affecting the resulting qualitative response.

3.2. Constitutive contact law between pairs of clay particles

The approach adopted in this work was to obtain the total normal force acting at the contact as the sum of a mechanical component and an electro-chemical component. A schematic representation of the normal and tangential contact laws introduced in this study is shown in Figure 3.

The mechanical component was modelled via the linear elastic-dissipative contact model in Equation 1, reported in Figure 3a as 'Mechanical force'. The values of k_n , k_t , k_{ro} and μ adopted in this work were assumed to be independent of the nature of the pore-fluid and are reported in Table 1. The selected values of k_n , k_t and k_{ro} guaranteed the simulation of 'stiff' particles in the pressure

range explored in this study (i.e. the ratio between the stiffness at the contact and the particle diameter is several orders of magnitude higher than the maximum applied pressure).

The electro-chemical component was modelled by introducing a long-range repulsive/attractive force between spheres not yet in contact, linearised for simplicity. The pattern of the electro-chemical component of the normal force is reported in Figure 3a as ‘Coulombian force’. The long-range Coulombian interaction, $f_{ij,Coul}^n$, arises for negative values of the overlap (representing the distance between spheres not in contact) once a fixed threshold value is exceeded, and remains constant after overlapping occurs:

$$f_{ij,Coul}^n = \begin{cases} 0, & \delta_{ij}^n < \delta_{ij}^{n,*} \\ k_{Coul}(\delta_{ij}^{n,*} - \delta_{ij}^n), & \delta_{ij}^{n,*} < \delta_{ij}^n < 0 \\ k_{Coul}(\delta_{ij}^{n,*}), & \delta_{ij}^n > 0 \end{cases} \quad 5$$

where $\delta_{ij}^{n,*}$ is the threshold overlap, and k_{Coul} is the normal stiffness of the long-range Coulombian interaction. The Coulombian force is positive (repulsive) when spheres i and j carry the same charge, and is negative (attractive) when spheres i and j carry opposite charges. Changing the sign of the Coulombian force allows for simulation of alkaline/acidic pore-fluid. Changing the value of k_{Coul} allows for simulations of pore-fluids with different dielectric permittivity.

Values of the normal Coulombian stiffness k_{Coul} for the simulation of different pore-fluids were selected following a rigorous calibration procedure against experimental results (described in Section 4.3). It is worth noticing that, as in Pedrotti and Tarantino (2017), Coulombian forces were assumed to be the only electro-chemical forces controlling the interaction between particles not yet in contact. However, the constitutive contact law could be easily extended to more complex contact interactions (e.g. including van der Waals forces) by considering additional attractive forces in the $\delta_{ij}^n < 0$ range.

The total normal force acting at the contact is then obtained by adding together the mechanical and electro-chemical contributions given by Equation 2 and Equation 5 respectively ('Total force' in Figure 3a):

$$f_{ij}^{n,tot} = f_{ij}^n + f_{ij,Coul}^n$$

6

Once the total force at each contact is calculated and the instantaneous position of the particles is known, macroscopic variables such as the distribution of the stress in the assembly could be extracted from the discrete data via the coarse-graining micro-macro transition method implemented in MercuryDPM (Weinhart et al., 2012; Tunuguntla, et al., 2015).

3.3. Design of clay-like particles

Two types of particles were designed in this work as shown in Figure 4. Particles that are negatively charged on both edge and face (alkaline pore fluid) were generated by assigning a negative charge to all the spheres belonging to each rod, resulting in the development of only repulsive long-range forces between rods interacting with each other. Particles that are negatively charged on the face and positively charged on the edge (acidic pore fluid) were generated by assigning a negative charge to the inner spheres of each rod and a positive charge to the end spheres. This choice resulted in the formation of edge-to-face contacts between rods, driven by the attractive force developing between positively charged edges and negatively charged faces.

4. NUMERICAL PROCEDURES

4.1. Specimen preparation

DEM simulations were performed on assemblies of $N_{rods}=300$ rods, amounting to a total number of spheres equal to 5700. The effect of the sample size was tested by performing preliminary

simulations on specimens with $N_{\text{rods}} = 200, 300, 500$ and 1000 rods, using the model parameters reported in Table 1 and a Coulombian stiffness $k_{\text{Coul}} = 0.5 \text{ N/m}$. Results were found to be independent of the rod number for $N_{\text{rods}} > 200$, leading to the conclusion that a specimen containing 300 rods is the smallest volume element that can accurately represent the overall behaviour on average.

Initial configurations were created by placing the rods in a square domain in the x-z plane. The domain boundaries were taken as solid walls, and the particle-to-wall interaction were assumed to be only mechanical. Preliminary tests were performed to assess the effect of solid boundaries by comparing the response of the entire specimen with the response of the inner core of the specimen. No noticeable differences were observed.

Rods were initially placed in the domain with their long axis along the x-direction. The x and z coordinates of the centre of the first sphere forming each rod were assigned randomly, while a constant y coordinate was assigned to the centres of all the spheres and remained unchanged during the entire simulation. The initial size of the domain was selected in order to obtain a specimen in a gas-like state, i.e. with a void ratio $e = 20$ and rods not interacting with each other. The void ratio of the specimen is intended here as the area fraction, i.e. the ratio between the area occupied by the voids and the area occupied by the solids obtained by projecting the rods onto the x-z plane.

Once the 'gas' specimen was created, a constant displacement rate was assigned to the top and right walls, and a position-dependent displacement rate was assigned to the particles in order to compress the specimen isotropically. The movement was stopped when the material experienced a fluid-solid transition, i.e. the virtual specimen was able to carry an external load. The signature of the transition is given by non-zero values of the stress and of the average number of contacts (including electro-chemical long-range contacts) within the specimen.

The assembly was then subjected to a relaxation stage (i.e. boundaries were kept stationary and the particles were left to relax towards an equilibrium configuration). In order to expedite the relaxation stage, an additional global background dissipation (reported in Table 1) proportional to the particle velocity was introduced. The relaxation stage was stopped when the kinetic energy of the sample was found to be at least five orders of magnitude smaller than the elastic energy.

4.2. 1-D compression and unloading

After relaxation, one-dimensional loading (compression) and unloading (rebound) of the specimen in the z-direction were performed by lowering or raising the top boundary wall respectively (displacement-controlled mode). During this stage, the void ratio e and the vertical stress state of the specimen σ'_z were calculated at regular intervals in order to obtain a compression curve.

During both loading and unloading paths, the displacement rate assigned to the top boundary (corresponding to a displacement of $1.6e-5 \mu\text{m}$ for each time step) was maintained small enough to ensure a quasi-static process. To this end, the displacement rate was selected by performing the same loading/unloading paths at different displacement rates and identifying the maximum displacement rate below which the output of the simulation became independent of the displacement rate itself. The addition of a background dissipation (smaller than the one used for relaxation and reported in Table 1) allowed to increase the displacement rate without affecting the results, thus reducing the total simulation time.

4.3. Calibration of the Coulombian normal stiffness

In order to reproduce the response of the clay specimens during 1-D compression, the parameters that characterise the Coulombian contact law need to be defined, namely the threshold overlap $\delta_{ij}^{n,*}$

and the normal Coulombian stiffness k_{Coul} . The threshold overlap $\delta_{ij}^{n,*}$ was tentatively selected as 1/2 of the rod thickness (as shown in Table 1) and assumed to be independent of the pore-fluid. On the other hand, the value of the normal Coulombian stiffness k_{Coul} was assumed to depend on the dielectric permittivity of the pore-fluid. The approach followed in this paper was to calibrate the Coulombian stiffness for water, k_{Coul}^{water} , against experimental data, whereas the Coulombian stiffness for acetone and air were derived theoretically.

The end of the preparation stage in the DEM simulation (corresponding to the fluid-solid transition, as described in Section 4.1) returns a value of void ratio that can be assumed as the initial void ratio of the virtual specimen, e_0^{DEM} . The initial void ratio depends in turn on the selected value of the model parameter k_{Coul} (i.e. the higher is the stiffness, the higher is the initial void ratio, as a result of the repulsion between charged particles). For the case of water as the pore-fluid, the stiffness k_{Coul}^{water} was calibrated by matching the initial void ratio of the virtual specimen, $e_{0,water}^{DEM}$, with the one measured experimentally at quasi-zero vertical stress ($e_{0,water}^{exp}$) by Pedrotti and Tarantino (2017):

$$e_{0,water}^{DEM} \equiv e_{0,water}^{exp} \quad 7$$

The values of k_{Coul} for the other two pore-fluids were instead calculated by assuming that the Coulombian force developing between charged particles is inversely proportional to the dielectric permittivity of the pore-fluid, ε (as shown in Equation 1). As a result, the Coulombian stiffness in acetone and air were scaled from the Coulombian stiffness in water via the dielectric permittivity:

$$k_{Coul}^{air} = \frac{(k_{Coul}^{water} \cdot \varepsilon^{water})}{\varepsilon^{air}} \quad 8$$

$$k_{Coul}^{acetone} = \frac{(k_{Coul}^{water} \cdot \varepsilon^{water})}{\varepsilon^{acetone}} \quad 9$$

where ε^{air} , $\varepsilon^{acetone}$ and ε^{water} are the relative permittivity values of air, acetone and water respectively ($\varepsilon^{air} = 1$, $\varepsilon^{acetone} = 25$, and $\varepsilon^{water} = 80$).

To sum up, only one value of the model parameter k_{Coul} was calibrated in this study against experimental data, i.e. k_{Coul}^{water} . The values of k_{Coul} in acetone and air were instead purposely derived on the basis of physicochemical considerations (Equations 8 and 9), in order to prove the soundness of the micromechanical framework. This is shown in details in Section 5, where the proposed model is validated against its ability to reproduce the initial void ratios for different pore-fluid dielectric permittivity values (Section 5.1), as well as their compression and unloading-reloading behaviour (Sections 5.2, 5.3, 5.4).

5. NUMERICAL RESULTS AND DISCUSSION

Four sets of simulations were performed by changing the contact law parameter k_{Coul} and the sign of the charge assigned to the spheres. These simulations were aimed at reproducing the experimental compression behaviour of the kaolin clay specimens tested by Pedrotti and Tarantino (2017) by considering pore-fluids with different dielectric permittivity (air, acetone, and water) and different pH (acidic pH and alkaline pH).

The association between the experimental tests and the numerical simulations is given in Table 2. Particle edges were given a positive charge in Simulations 1, 2 and 3 to generate an edge-to-face configuration as observed experimentally in Tests 1, 2, and 3 for the case of air, acetone, and acidic water respectively. Particle edges were given a negative charge in Simulations 4 to generate a face-to-face configuration as observed experimentally in Test 4 for the case of alkaline water.

5.1. Validation of the contact law for clays

The core of the contact law for clays is represented by the Coulombian force, which was added to the traditional mechanical force implemented in granular DEM analyses. In turn, the Columbian force was designed based on the assumption that its magnitude and sign depend on the dielectric permittivity of the pore-fluid and on the pH. The contact law can therefore be probed by comparing the response of the DEM model with the experimental results in Pedrotti and Tarantino (2017) for different permittivity and pH.

Figure 5 shows the values of the simulated and experimental initial void ratio e_0 at the end of the preparation of the specimens. According to the calibration procedure previously described, the initial void ratio for the case of water at pH = 4 (Simulation 3) obviously matches the void ratio measured experimentally at quasi-zero vertical stress.

The striking result is that the void ratio is matched reasonably well at a quantitative level also for the other pH/dielectric permittivity scenarios. The initial void ratio matched almost perfectly for the case of the edge-to-face configuration (Simulation 1 and 2). For the case of the face-to-face configuration (Simulation 4), the substantial reduction in the initial void ratio caused by the de-activation of most of the edge-to-face contacts for the case of alkaline pore-fluid is also well captured. There is indeed a slight underestimation of the void ratio by the DEM simulation. This may be due to the fact that the variation of pH from 4 to 9 in real clay specimens is unlikely to cause the deletion of all the positive edge charges, resulting in a slightly more open structure due to residual edge-to-face contacts.

The ability to predict the initial configuration of the specimen at a quantitative level in terms of void ratio by relating a microscopic quantity (k_{Coul}) with a macroscopic quantity (ε) is the first demonstration of the validity of the DEM model to capture some aspects of the macroscopic behaviour of clayey materials, even using simplified contact laws.

5.2. Effect of pre-consolidation stress on 'elastic' response upon unloading

Wide experimental evidence shows that the unloading-reloading lines of clay specimens in the plane ($e - \log \sigma'_z$) are not parallel but increase their slope as the pre-consolidation stress increases. This is also the case for the specimens saturated with ordinary laboratory water and subjected to standard oedometer tests shown in Figure 6 (Pedrotti and Tarantino, 2017).

The DEM model was therefore challenged for its capability to capture the effect of the pre-consolidation stress on the elastic behaviour upon unloading/reloading. Figure 7 shows the results of Simulation 3, where three unloading paths starting at different values of σ_z were performed. The increase in the slope of the unloading paths with the maximum stress experienced by the assembly before unloading appears to be captured satisfactorily, in line with the experimental observation.

It should be noted that the experimental compression curve cannot be compared quantitatively with the DEM simulation. The range where the void ratio appears to be linear in a semi-log scale (i.e. the range where e decreases exponentially with σ_z) extends up to 10 kPa in the DEM simulation, whereas the experimental data shows that this range is equal to or greater than 2000 kPa. Furthermore, simulated kaolin particles have been observed to bend significantly after the 10 kPa range is exceeded (as shown later on in Figure 12), suggesting that the response of the model at high stress may be unreliable. The experimental compression curve should therefore only be compared with the linear branch of the simulated compression curve in the plane ($e - \log \sigma_z$). The mismatch in the vertical stress can be attributed to the simplifications introduced in this DEM analysis. For instance, the mechanical interaction and the Columbian interaction of the contact law were designed as piecewise linear functions, although a Hertzian contact law and a non-linear function reproducing the DLVO theory (combined effect of van der Waals and double layer forces) would in principle be more appropriate. However, highly non-linear contact laws would increase the computational time significantly. Since this work is mainly aimed at validating the conceptual

micromechanical model underlying the presented DEM model, simple contact laws able to reach this aim in a short computational time were preferred at this stage.

It is interesting to exploit the DEM model to explore the micro-mechanisms controlling the response observed in Figure 6 and Figure 7. Figure 8 shows the configuration of the specimen at different stages of the loading- unloading process (points A, B, C, B' and C' in Figure 7): state A represents the state at the end of the preparation stage, state B and C represent states on the virgin compression line at two different values of pre-consolidation stress, and B' and C' represent two states at the end of unloading.

At the end of the preparation stage (A), rods are arranged in both edge-to-face and face-to-face configurations, resulting in the creation of a relatively open structure. The bigger pores are associated with the formation of edge-to-face contacts. The smaller pores correspond instead to the gaps between sub-parallel particles.

Upon virgin loading (A – B – C), three different micro-mechanisms are clearly visible (Figure 8a):

- i) the reduction of the distance between particles in face-to-face configuration (i.e. mechanism 'i' in Figure 1 and 8a);
- ii) the rotation of particles in edge-to face contact configuration towards each other without contact disengagement (i.e. mechanism 'ii' in Figure 1 and 8a);
- iii) the loss of edge-to-face contacts, in turn generating a face-to-face configuration (i.e. mechanism 'iii' in Figure 1 and 8a).

At the onset of compression (path A – B in Figure 7 and Figure 8a), the specimen compressibility appears to be mostly associated with mechanisms 'ii', as particles in the edge-to-face configuration are brought closer to each other by the external load (reversible mechanism). At

higher stress (path B – C in Figure 7 and Figure 8a), compression appears to be dominated by mechanism 'iii', as the volume change generated by the loss of edge-to-face contacts (non-reversible mechanism) is much higher than the one associated with mechanism 'i' and 'ii'. From C onwards (Figure 7 and Figure 8a), compression gradually starts to be dominated by mechanism 'i', i.e. the reduction of the distance between sub-parallel particles (reversible mechanism), as face-to-face configuration becomes predominant.

Upon unloading (B – B', C – C') (Figure 7 and Figure 8b and 8c), the elastic behaviour is associated with different mechanisms depending on the magnitude of the pre-consolidation stress. At low pre-consolidation stress (B – B'), particles in both edge-to-face and face-to-face configuration undergo a small elastic rebound, due to the small Coulombian repulsion activated in 'i' and 'ii' upon loading. The particle configuration of the specimen remains essentially unaltered during unloading.

As the pre-consolidation stress increases (C – C'), the edge-to-face contacts still existing in the assembly do not contribute to the rebound, i.e. their 'structure' remains totally unaltered after unloading. It appears that the particle 'frame' generated by the edge-to-face contacts is surrounded by a 'matrix' of particles in face-to-face configuration, which almost loads the particle frame isotropically. The elastic rebound is therefore mostly associated with the rebound of particles in face-to-face configuration. The high Coulombian repulsion due to the high stress reached upon loading in turn generates a higher rebound upon unloading.

Finally, it is worth noticing that the loss of edge-to-face contacts is indeed permanent (as in Figure 1): edge-to-face contacts lost upon loading are not recovered upon unloading.

5.3. Effect of dielectric permittivity on one-dimensional compression behaviour

The second aspect explored in the DEM analyses concerns the effect of the dielectric permittivity of the pore-fluid on the one-dimensional compression of clay. The experimental results of oedometer tests conducted on kaolin clay specimens saturated with air (dry powder, $\varepsilon = 1$), acetone ($\varepsilon = 25$) and laboratory water ($\varepsilon = 80$) are shown in Figure 9.

The numerical results of Simulation 1, 2, and 3 are shown in Figure 10a and 10b for loading (non-reversible volume change) and unloading (reversible volume change) respectively. The variation of the long-range Coulombian interaction between particles as induced by the change in dielectric permittivity affects the macroscopic behaviour of the assembly upon both loading and unloading. Upon loading, the higher is k_{Coul} (i.e. the lower is ε) the higher is the slope of the virgin compression curve. Upon unloading, the higher is k_{Coul} , the lower is the slope of the unloading 'elastic' line.

The response of the DEM model captures very well the behaviour observed experimentally (at a qualitative level). The agreement goes beyond a purely visual comparison. Figure 11 shows the comparison in terms of compressibility index C_c and swelling index C_s normalised with respect to their values in 'ordinary' water (pH= 4, Simulation 3). As shown in Figure 9 and 10, the indexes were obtained as the slope of linear functions interpolating the data in the linear branch of the compression curves. A very good agreement is observed between experimental and simulated values.

The DEM model was again used to explore the micro-mechanisms leading to this macroscopic behaviour. Figure 12 shows some of the specimen configurations obtained from Simulation 2 (acetone, $\varepsilon = 25$), and 3 (water, $\varepsilon = 80$). Pictures of the assemblies were taken at different stages: at the end of the preparation stage (A and E for water and acetone respectively), at an intermediate

stage during first loading (C for water, F for acetone), and at two intermediate states upon unloading (D – D' for water and G – G' for acetone).

The effect of the magnitude of the Coulombian stiffness k_{Coul} on the specimen configuration at the same stress is clearly visible. The higher is k_{Coul} , the more open is the structure of the assembly (A and E). Upon first loading (A – C and E – F in Figure 10a and Figure 12), the higher compressibility of the specimen in Simulation 2 (pore-fluid = acetone) is associated with mechanism 'iii'. The more open is the structure, the higher is the loss in terms of void ratio every time an edge-to-face contact is permanently lost upon first loading, leading to a faster reduction of void ratio with applied load.

Upon unloading (D – D' and G – G' Figure 10b and Figure 12), the higher rebound of the specimen in Simulation 3 (pore-fluid = water) is associated with mechanisms 'i' and 'ii', i.e. the reduction of the distance between particles in both edge-to-face and face-to-face configuration before unloading. This behaviour can be easily explained by considering two qualitative contact laws with different slopes k_{Coul} , as is the case for Simulation 2 and 3 (Figure 13). For particles interacting in the $\delta_{ij}^n < 0$ range, let us assume that the same change in external stress upon unloading (for example from D – D' and G – G'), also produces the same change in normal contact force, Δf . The resulting change in overlap $\Delta\delta$ depends on the Coulombian stiffness, in particular it is higher for the contact characterised by lower stiffness and, hence, higher dielectric permittivity (i.e. water).

5.4. Effect of pH on compression behaviour

The validity of the DEM model against its ability to simulate the effect of pH on the compression behaviour of clay was explored by comparing the numerical results of Simulation 3 and 4 with the

experimental results of oedometer tests performed on kaolin clay specimens saturated with ordinary deionised water (pH = 4) and alkaline water (pH = 9) (Figure 14 and 15).

The case of pH=9 was simulated by substituting the positive charge on the edges of the rods with a negative charge. As shown in Figure 15, this caused a drastic reduction of the void ratio at the same vertical stress, and reduced the specimen compressibility upon first loading. Upon unloading, the numerical response observed in Simulation 4 (pH=9) returns a small plastic deformation.

Figure 16 shows the comparison between the results obtained experimentally and numerically in terms of compressibility index C_c and swelling index C_s normalised with respect to their values in ordinary water (pH= 4, Simulation 3). Again, the trend observed in the experimental data is well captured by the simulation.

The underlying micromechanics behind the macroscopic behaviour at different pH levels was explored by comparing the assembly configurations obtained from Simulation 3 and 4 (Figure 17). The formation of edge-to-face contacts present in Simulation 3 does not occur in Simulation 4, where rods are arranged in sub-parallel configurations even at low stresses (A and H).

Upon first loading (A – C and H – I in Figure 15a and Figure 17), the lower compressibility observed in Simulation 4 is associated with the absence of edge-to-face contacts: the rods are arranged into a closer configuration at the beginning of compression, and the resulting microstructure is less compressible since there are no edge-to-face contacts that are permanently lost upon first loading.

Upon unloading, the response observed numerically in Simulation 4 shows that the loading and unloading paths overlap almost completely, except at very low stresses. The small plastic deformation occurring at the end of the unloading path (point M in Figure 15b and Figure 17) is only associated with a slight rearrangement of the rods during first loading. In this case, plastic

deformation arises from irreversible particle rearrangement as opposed to the plastic deformation observed in water at pH = 4, which is mainly controlled by the disengagement of the edge-to-face contact.

5.5. Evolution of fabric during one-dimensional compression

The particle-scale data was further processed to explore the evolution of fabric during one-dimensional compression, thus corroborating the qualitative analysis of particle configurations presented in the previous Sections. To this end, the components F_{ij} of the fabric tensor \mathbf{F} were defined according to Oda et al. (1985):

$$F_{ij} = \frac{1}{N_{rods}} \sum_{k=1}^{N_{rods}} n_i^{(k)} n_j^{(k)} \quad 8$$

where $n_i^{(k)}$ ($i, j = x, z$) are the direction cosines of the unit vector $\mathbf{n}^{(k)}$ oriented with the main axis of the k-th rod, and N_{rods} is the total number of rods in the domain volume. Each component of the fabric tensor varies between 0 and 1 (e.g. horizontally-oriented rods would result in $F_{xx} = 1$ and $F_{xz} = F_{zz} = 0$, and vertically-oriented rods would result in $F_{xx} = F_{xz} = 0$ and $F_{zz} = 1$). The fabric tensor was calculated only up to the value of σ_z preceding the loading-induced rod bending (as shown in Figure 12, points D and G). The fabric deviator ($F_{xx} - F_{zz}$) was adopted in this work to characterise the fabric anisotropy. The fabric deviator varies between -1 and 1, as Equation 8 implies that $F_{xx} + F_{zz} = 1$. An isotropic sample is characterized by $(F_{xx} - F_{zz}) = 0$.

The evolution of the fabric deviator upon loading for Simulation 1, 2, 3 and 4 is shown in Figure 18. For clarity, the compression curves within the selected stress range are also reported in the figure (Figure 18a).

At the onset of compression, the fabric deviator in Figure 18b is greater than zero for all the specimens, i.e. the horizontal orientation prevails on the vertical orientation. This is as a result of

the preparation history, as rods are initially introduced horizontally in a gas-state and then rearrange as the inter-particle interactions become active. However, the initial anisotropy of the simulated specimens is considered to be realistic, as it resembles the slight anisotropy towards the horizontal direction observed in both natural clays (e.g. Zhu et al., 2013) and remoulded kaolin clay specimens (e.g. Sachan, 2008).

The specimen in Simulation 1 (air-like, $\varepsilon = 1$) is characterised by the lowest initial value of the fabric deviator (0.33), indicating that this specimen is characterised by the lowest degree of anisotropy (i.e. randomly oriented particles) due to the high Coulombian repulsion. The fabric deviator remains almost constant up to 40 kPa, i.e. no significant particle rearrangements occur within the specimen. This behaviour can be attributed to the activation of mechanisms 'i' and 'ii' (reversible compression of sub-parallel particles and particles in edge-to-face configuration with no contact disengagement), giving rise to reversible volume changes and negligible microstructural variations. For $\sigma_z > 40$ kPa, the fabric deviator increases as particles in edge-to-face configuration start to disengage (mechanism 'iii'), giving rise to non-reversible volume changes and, hence, the 'collapse' of the specimen microstructure.

The specimens in Simulation 2 (acetone-like, $\varepsilon = 25$) and Simulation 3 (water-like, $\varepsilon = 80$) are instead characterised by an intermediate (0.4) and high (0.44) initial value of the fabric deviator respectively, in line with the qualitative inspection of particle configurations in Figure 12 (configurations A and E). The increase of the fabric deviator, which indicates the activation of mechanism 'iii', occurs at lower stress values ($\sigma_z \approx 3$ kPa for Specimen 2 and $\sigma_z \approx 2$ kPa for Specimen 3), thus clearly indicating the dependence of the specimen irreversible compressibility upon the magnitude of the Coulombian repulsion. Furthermore, a clear plateau is visible in Simulation 3 at $\sigma_z \approx 6$ kPa, corresponding to the transition to a stable configuration almost insensitive to further stress changes. This behaviour is once again attributed to the reversible

mechanisms 'i' and 'ii', i.e. particles are 'elastically' brought closer to each other by the external load with no significant variation of the microstructure.

As for Simulation 4 (water at pH = 9), the absence of edge-to-face contacts (as shown in Figure 17) results in a significantly higher value of the initial fabric deviator, which remains almost constant upon loading because of the little rearrangement of the particles and the absence of irreversible mechanisms (the fabric deviator varies from 0.74 to 0.83, in contrast to Simulation 3 where the fabric deviator varies from 0.44 to 0.60).

Finally, Figures 19 and 20 show the histograms of particle orientations α (intended here as the angle between the rod main axis and the horizontal direction) at quasi-zero vertical stress and at $\sigma_z = 10$ kPa for different dielectric permittivity (Simulation 2 and 3) and pH (Simulation 3 and 4) respectively. At quasi-zero vertical stress (Figure 19a), the percentage of sub-horizontal particles (characterised by an orientation between 0° and 20°) is lower for acetone than water (37% in Simulation 2 against 42% in Simulation 3), in line with the initial values of the fabric deviator. At $\sigma_z = 10$ kPa (Figure 19b), the percentage of sub-horizontal particles increases for both simulations as the face-to-face configuration becomes predominant due to external loading (from 37% to 50% in Simulation 2, and from 42% to 57% in Simulation 3).

As expected, the difference in the percentage of sub-horizontal particles is more significant when comparing specimens with different pH values (Simulation 3 and 4), due to the de-activation of the edge-to-face contacts when moving from pH = 4 to pH = 9. In this case, the percentage of sub-horizontal particles is equal to 42% in Simulation 3 against 63% in Simulation 4 at quasi-zero vertical stress (Figure 20a), and 57% in Simulation 3 against 74% at $\sigma_z = 10$ kPa (Figure 20b).

6. CONCLUSIONS

This paper has presented a two-dimensional DEM framework for the simulation of assemblies of clay-like particles. This framework was aimed at validating a conceptual micromechanical model for non-active clays designed on the basis of indirect experimental evidence at the microscale.

The DEM model was designed around two main features. Firstly, assemblies of spherical primary units were created to form rod-shaped elements in order to mimic the elongated shape of clay particles. Secondly, attractive and repulsive long-range forces were added to the basic linear-elastic contact laws to simulate the electro-chemical interactions driven by the positive/negative charge distribution characterising the surface of the clay particles. The contact laws introduced in this work were tested against their ability to reproduce qualitatively key aspects of the macroscopic compression behaviour of kaolin clay observed experimentally by Pedrotti and Tarantino (2017) for different pH and dielectric permittivity of the pore-fluid.

The DEM analyses were based on a simple and physically-based calibration procedure. The absolute value of the stiffness associated with the Coulombian interaction, k_{Coul} , was calibrated against the experimental data for only one of the four pore-fluids (i.e. acidic water). The values of k_{Coul} for acetone and air (i.e. fluids having different dielectric permittivity) were then derived by scaling the Coulombian stiffness in acidic water by the dielectric permittivity of acetone and air respectively. For the alkaline pore-water, the value of k_{Coul} derived for acidic water was maintained, but only positive (repulsive) stiffness was considered.

A very good qualitative agreement was observed between the experimental data and the results of four sets of simulations in terms of a) the dependency of the slope of the unloading-reloading lines on the pre-consolidation stress, and b) the overall compression behaviour upon virgin loading and unloading-reloading.

The conceptual micromechanical model underlying the DEM framework was further explored via the qualitative inspection of particle configurations and quantitative analysis of fabric anisotropy and particle orientation. The occurrence of three main mechanisms occurring during compression clearly emerged from the DEM model, that is: i) the reduction of the distance between particles in face-to-face configuration, ii) the rotation of particles in edge-to-face contact with no contact disengagement, and iii) the permanent loss of edge-to-face contacts.

The DEM model was intentionally kept simple (2D environment, piecewise linear contact laws, and monodisperse grain size distribution) to demonstrate the robustness of the micromechanical concept underlying the contact laws. It is anticipated that a satisfactory quantitative prediction would be achieved by moving to a 3D environment, by considering polydisperse specimens, and by refining the contact laws.

ACKNOWLEDGEMENTS

The authors would like to thank the Multi Scale Mechanics group at the University of Twente (Enschede, the Netherlands), in particular Dr Kit Windows-Yule for his contribution to the implementation of the newly designed contact law for clay particles using MercuryDPM.

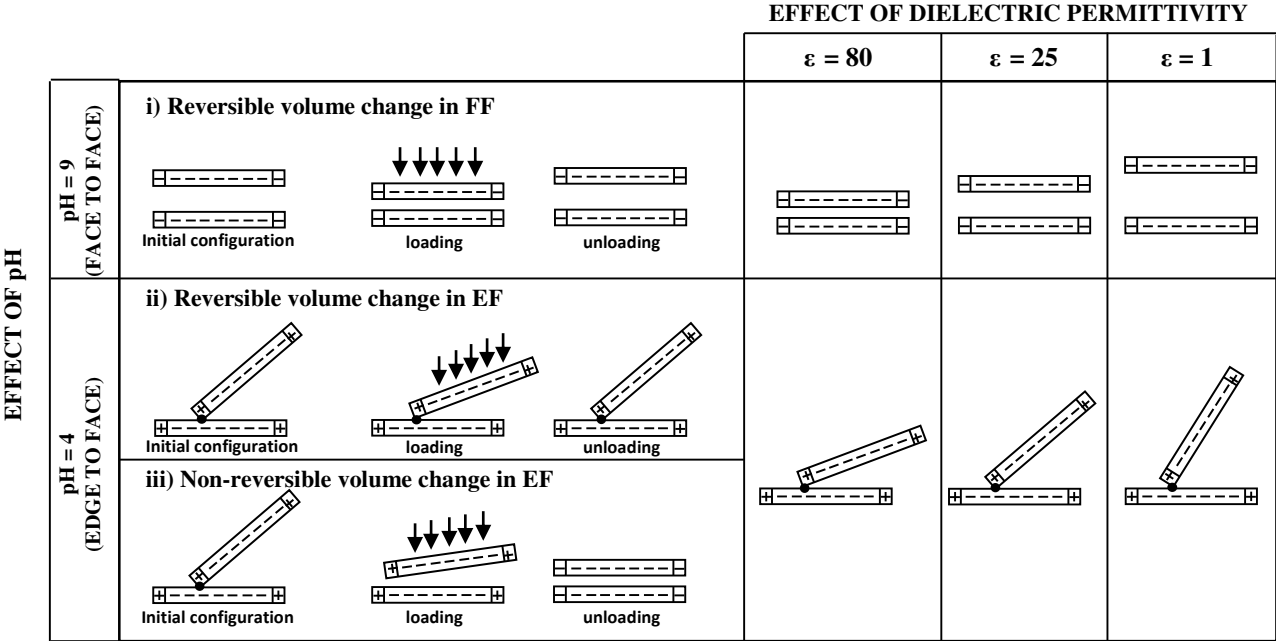
7. REFERENCES

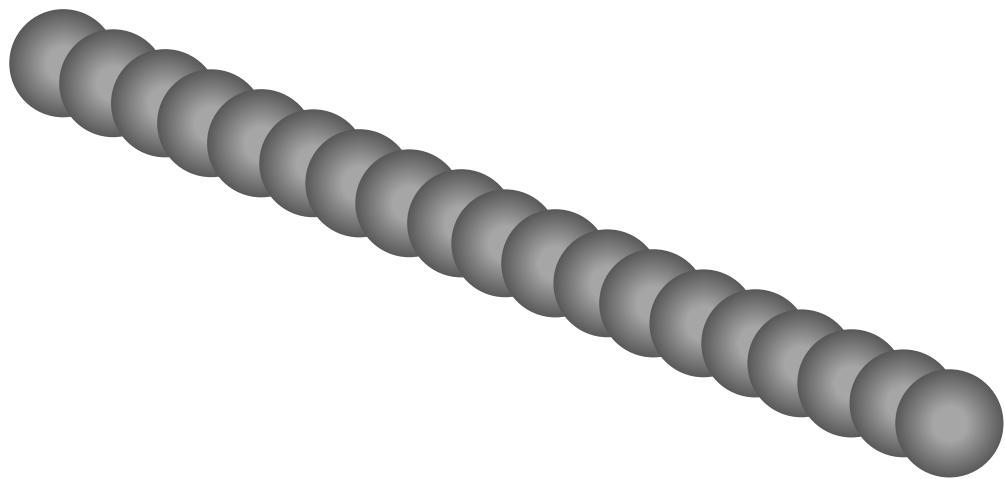
- Anandarajah, A., 2000. Numerical simulation of one-dimensional behaviour of a kaolinite. *Géotechnique*, 50(5), pp. 509-519.
- Anandarajah, A. & Amarasinghe, P. M., 2012. Discrete-element study of the swelling behaviour of Na-montmorillonite. *Géotechnique*, <http://dx.doi.org/10.1680/geot.12.P.012>.
- Anandarajah, A. & Chen, J., 1997. Van der Waals attractive force between clay particles in water and contaminants. *Soils and foundations*, 37(2), pp. 27-37.
- Andò, E. et al., 2012a. Experimental micromechanics: grain-scale observation of sand deformation. *Géotechnique, Lett.* 2(3), pp. 107-112. (Magnanimo, et al., 2008)
- Andò, E. et al., 2012b. Grain-scale experimental investigation of localised deformation in sand: a discrete particle tracking approach. *Acta Geotechnica*, 7(1), pp. 1-13.
- Asabi, M., Mahboudi, A., Thoeni, K., 2018. Discrete modeling of sand–tire mixture considering grain-scale deformability. *Granular Matter*, 20: 18. <https://doi.org/10.1007/s10035-018-0791-4>.
- Bolton, M. D., Nakata, Y. & Cheng, Y. P., 2008. Micro- and macro-mechanical behaviour of DEM crushable materials. *Géotechnique*, 58(6), pp. 471-480.
- Cavarretta, I., Coop, M. R. & O' Sullivan, C., 2010. The influence of particle characteristics on the behaviour of coarse grained soils. *Géotechnique*, 60(6), pp. 413-423.
- Cheng, Y. P., Nakata, Y. & Bolton, M. D., 2003. Discrete element simulation of crushable soil. *Géotechnique*, 53(7), p. 633–641.
- Cundall, P. A. & Strack, O. D. L., 1979. A discrete numerical model for granular assemblies. *Géotechnique*, 29(1), p. 47–65.
- Ebrahimi, D., Whittle, A. J., & Pellenq, R. J. M. 2016. Mesoscale properties of clay aggregate from potential of mean force representation of interactions between nanoplatelets. *J. Chem. Phys.*, 140.

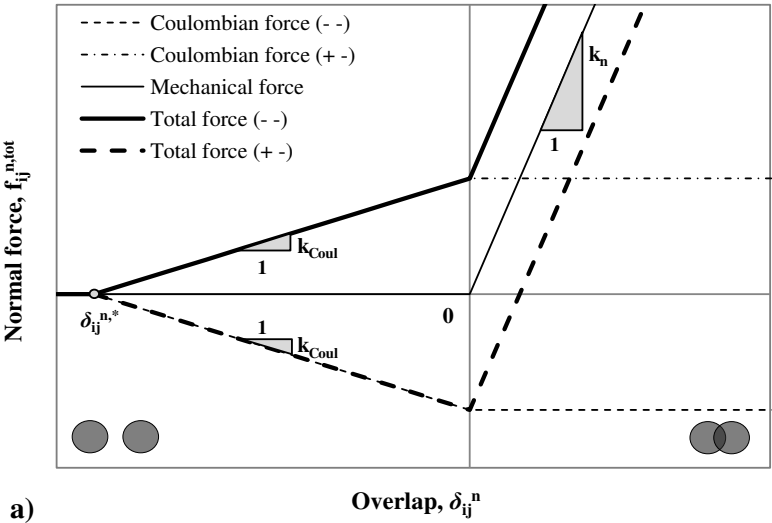
- Ebrahimi, D., Pellenq, R. J. M. & Whittle, A. J., 2016. Mesoscale simulation of clay aggregate formation and mechanical properties. *Granular Matter*, 18(49).
- Guo, N. & Zhao, J., 2012. The signature of shear-induced anisotropy in granular media. *Computers and Geotechnics*, Volume 47, pp. 1-15.
- Iwashita, K. & Oda, M., 1997. Rolling resistance at contacts in simulation of shear band development by DEM. *Journal of Engineering Mechanics*, 124(3), p. 285–292.
- Kawamoto, R., Andò, E., Viggiani, G. & Andrade, J. E., 2018. All you need is shape: Predicting shear banding in sand with LS-DEM. *Journal of the Mechanics and Physics of Solids*, Volume 111, pp. 375-392.
- Luding, S., 2008. Cohesive, frictional powders: contact models for tension. *Granular Matter*, <https://doi.org/10.1007/s10035-008-0099-x>
- Magnanimo, V. et al., 2008. Characterizing the shear and bulk moduli of an idealized granular material. *EPL (Europhysics Letters)*, 81(3).
- Mitchell, J. & Soga, K., 2005. *Fundamentals of soil behavior*. Hoboken, NJ, USA: John Wiley and Sons Inc.
- Mouraille, O., 2009. Sound propagation in dry granular materials : discrete element simulations, theory, and experiments. PhD thesis.
- O' Sullivan, C., Bray, J. D. & Cui, L., 2006. Experimental validation of particle-based discrete element methods. *GeoCongress 2006*, [https://doi.org/10.1061/40803\(187\)5](https://doi.org/10.1061/40803(187)5).
- O'Donovan, J., O'Sullivan, C. & Marketos, G., 2012. Two-dimensional discrete element modelling of bender element tests on an idealised granular material. *Granular matter*, 14(6), p. 733–747.
- Oda, M., Nemat-Nasser, S. & Konishi, J., 1985. Stress-induced anisotropy in granular masses. *Soils and Foundations*, 25(3), pp. 85-87.
- Pedrotti, M. & Tarantino, A., 2017. An experimental investigation into the micromechanics of non-active clays. *Géotechnique*, <http://dx.doi.org/10.1680/jgeot.16.P.245>.

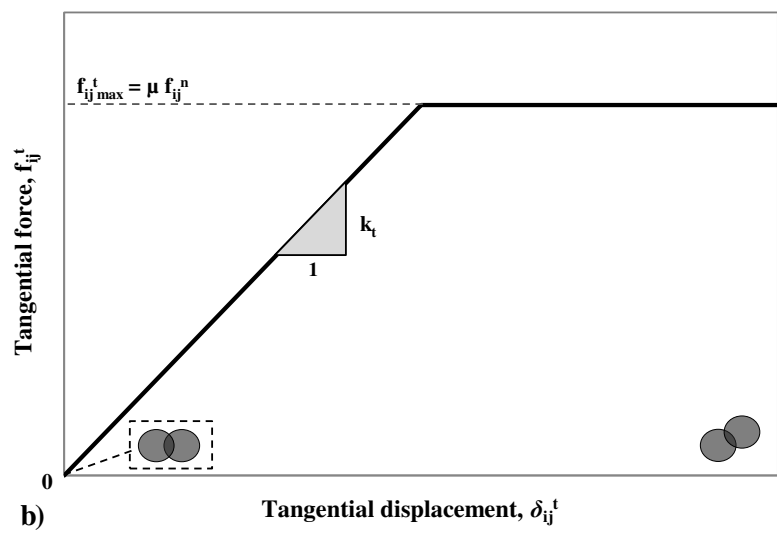
- Sachan, A., 2008. Use of atomic force microscopy (AFM) for microfabric study of cohesive soil. *Journal of Microscopy*, Volume 232, pp. 422-431.
- Sjoblom, K. J., 2015. Coarse-grained Molecular Dynamics approach to simulating clay behaviour. *Journal of Geotechnical and Geoenvironmental Engineering*, 142(2).
- Thornton, C., Yin, K. K. & Adams, M. J., 1996. Numerical simulation of the impact fracture and fragmentation of agglomerates. *J. Phys. D: Appl. Phys*, Volume 29, p. 424-435.
- Tunuguntla, D. R., Thornton, A. R. & Weinhart, T., 2015. From discrete elements to continuum fields: Extension to bidisperse systems. *Comp. Part. Mech.*, DOI 10.1007/s40571-015-0087-y.
- Ueda, T., Matsushima, T., Yamada, Y., 2013. DEM simulation on the one-dimensional compression behavior of various shaped crushable granular materials. *Granular Matter*, 15(5), pp. 675-684.
- Weinhart, T., Thornton, A. R., Luding, S., Bokhove, O., 2012. From discrete particles to continuum fields near a boundary. *Granular Matter*, 14(2), pp. 289-294.
- Weinhart, T., Tunuguntla, D. R., van Schrojenstein-Lantman, M. P. , van der Horn, A. J., Denissen, I. F. C., Windows-Yule, C. R., de Jong, A. C., Thornton, A. R., 2016. MercuryDPM : a fast and flexible particle solver part A : Technical Advances. *Proceedings of the 7th International Conference on Discrete Element Methods*, pp. 1353-1360.
- Weinhart, T., Tunuguntla, D. R., van Schrojenstein Lantman, M. P., Denissen, I. F. C., Windows-Yule, C. R., Polman, H., Tsang, J. M. F., Jin, B., Orefice, L., van der Vaart, K., Roy, S., Shi, H., Pagano, A. G., den Breeijen, W. M., Scheper, B. J., Jarray, A., Luding, S., Thornton, A. R., 2017. MercuryDPM : a fast and flexible particle solver part B : Applications. *5th International Conference on Particle-Based Methods - Fundamentals and Applications, PARTICLES 2017*.
- Yao, M. & Anandarajah, A., 2003. Three-Dimensional Discrete Element Method of analysis of clay. *J. Eng. Mech*, Volume 129, pp. 585-596.

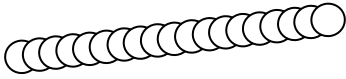
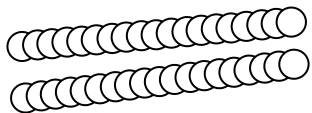
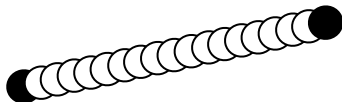
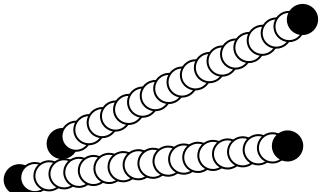
Zhu, Q., Jin, Y., Yin, Z. & Hicher, P. Y., 2013. Influence of natural deposition plane orientation on
oedometric consolidation behavior of three typical clays from southeast coast of China. J Zhejiang Univ-Sci
A (Appl Phys & Eng), 14(11), pp. 767-777.

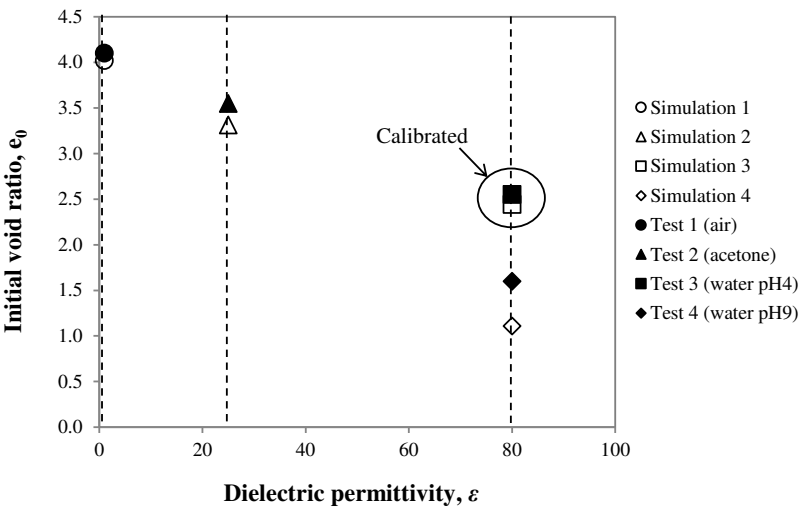


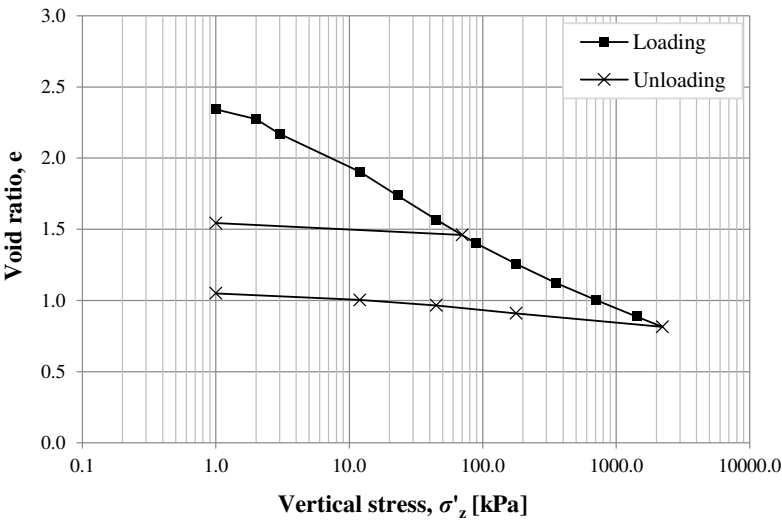


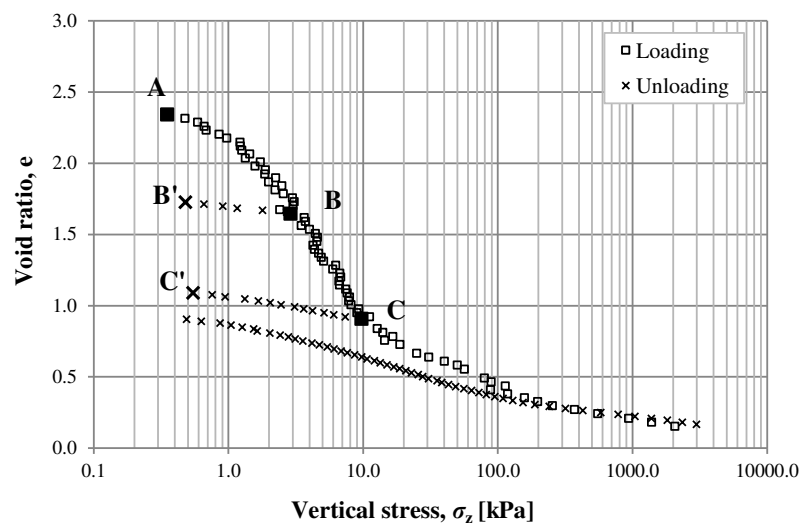


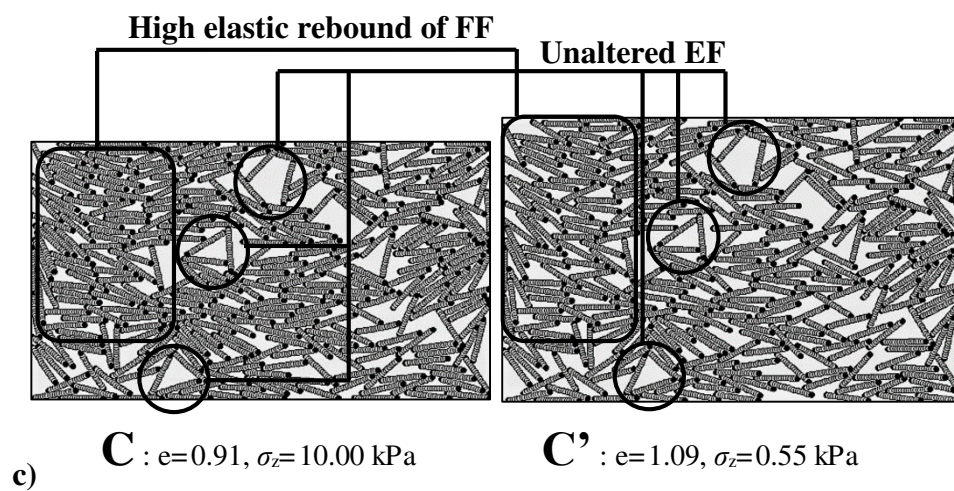
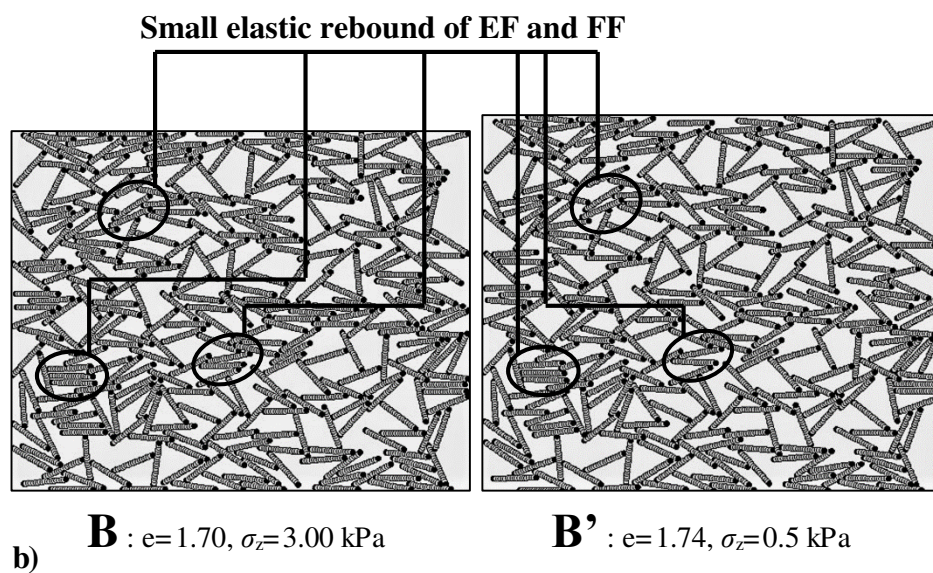
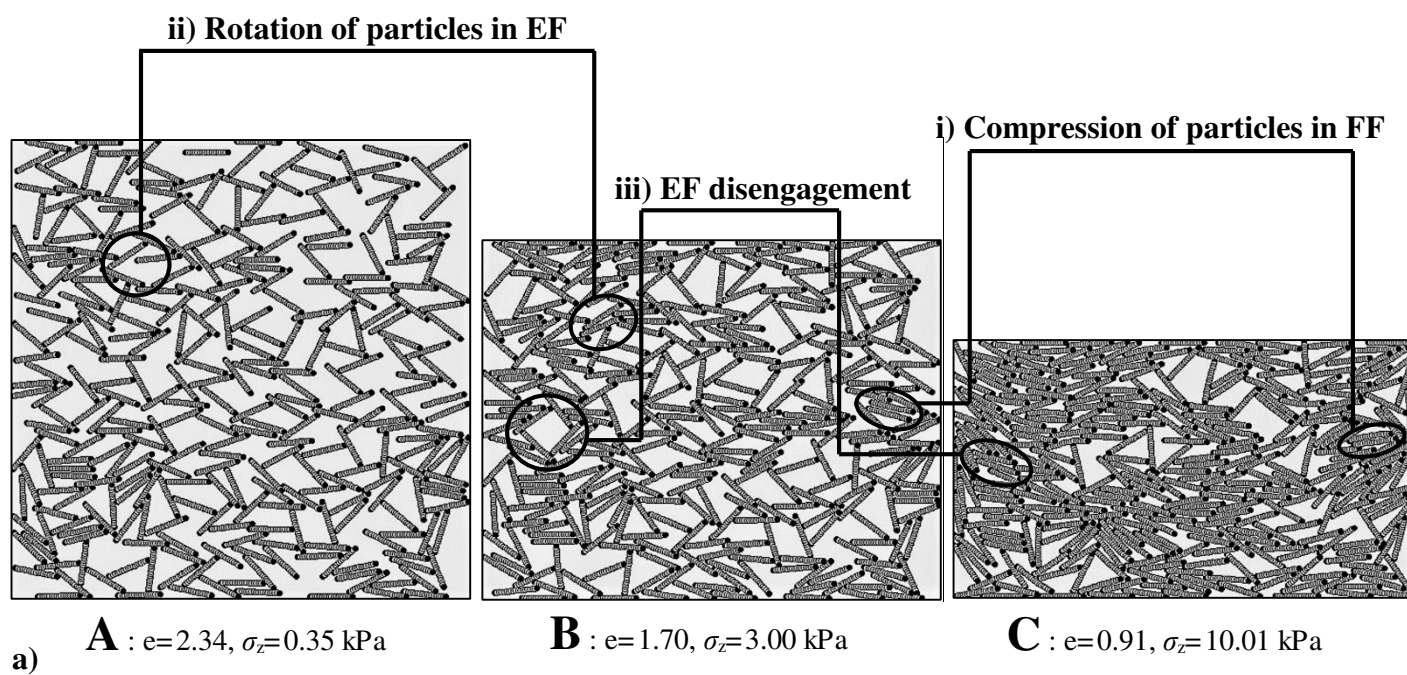


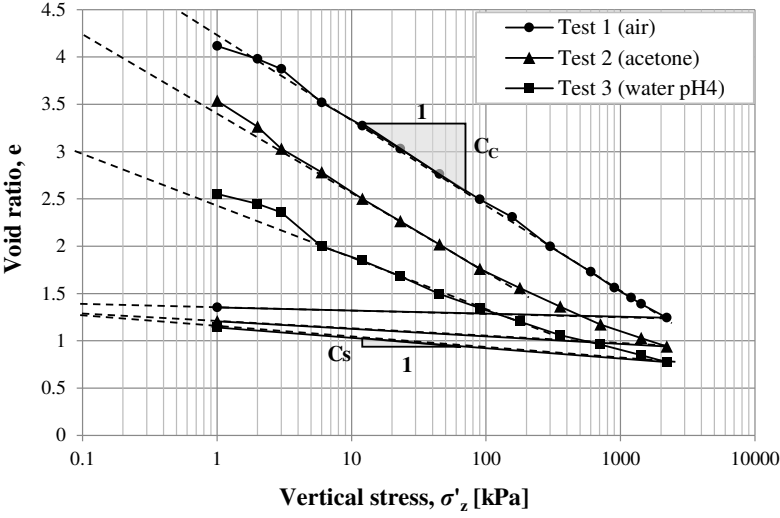
<p>pH = 9</p>	<p>— ○ Negative charge</p> 	<p>FACE TO FACE</p> 
<p>pH = 4</p>	<p>— ○ Negative charge + ● Positive charge</p> 	<p>EDGE TO FACE</p> 

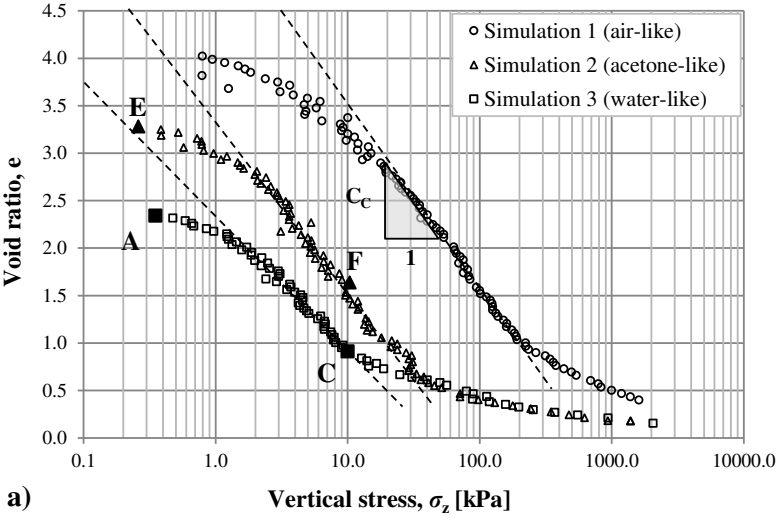


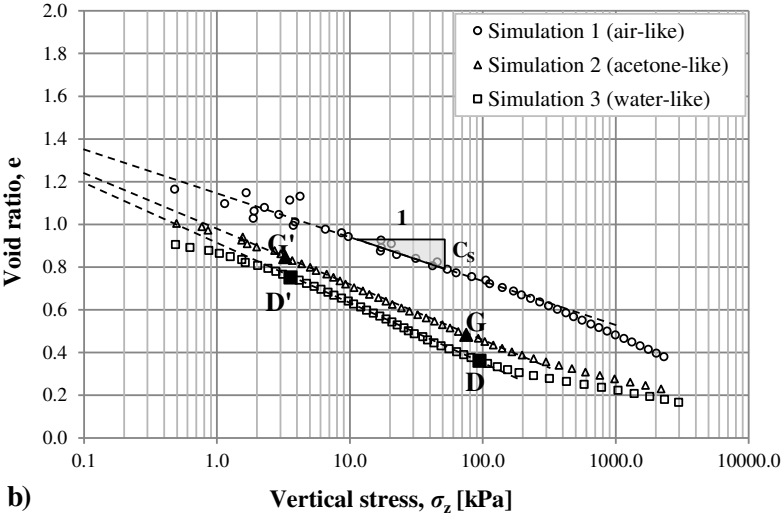


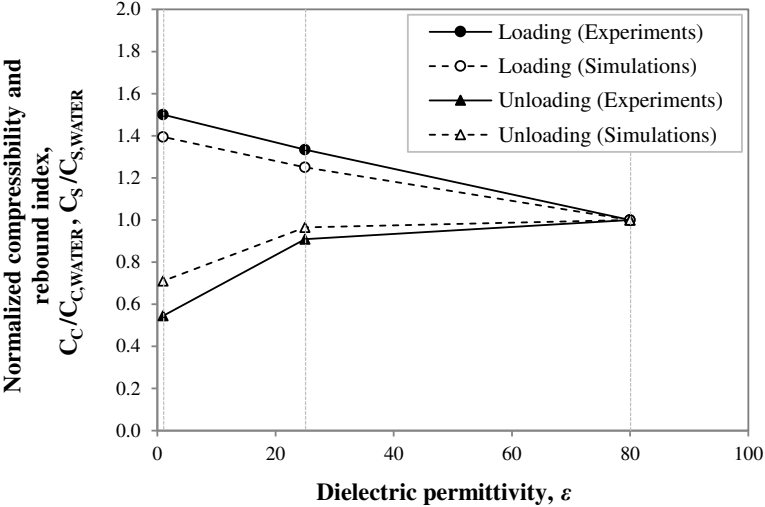




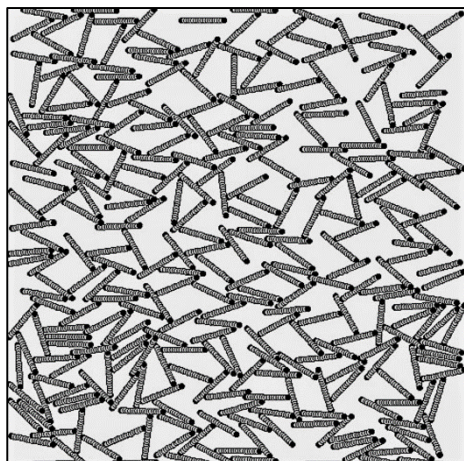




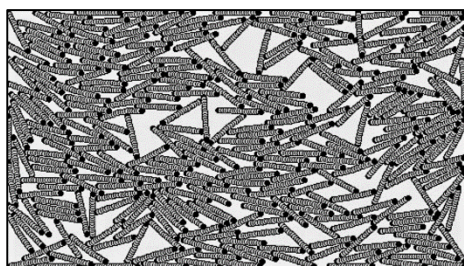




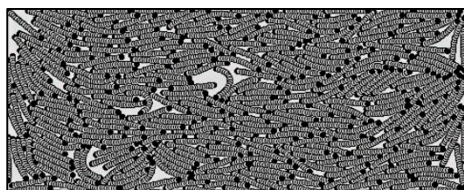
Simulation 3 (water pH4)



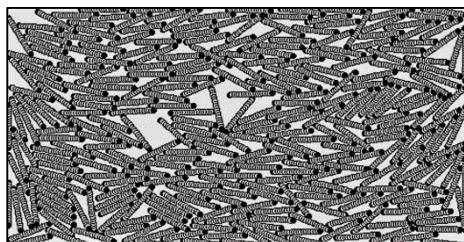
A : $e=2.34$, $\sigma_z=0.35$ kPa



C : $e=0.91$, $\sigma_z=10.01$ kPa

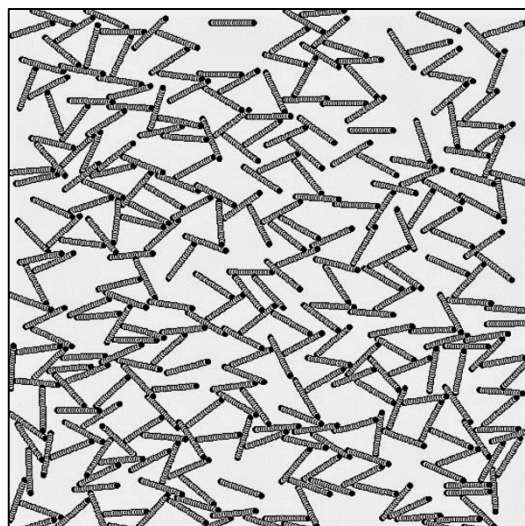


D : $e=0.36$, $\sigma_z=94.7$ kPa

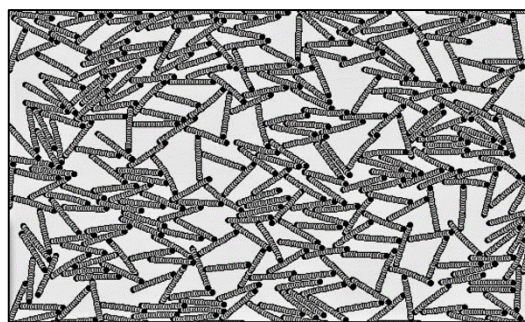


D' : $e=0.75$, $\sigma_z=3.57$ kPa

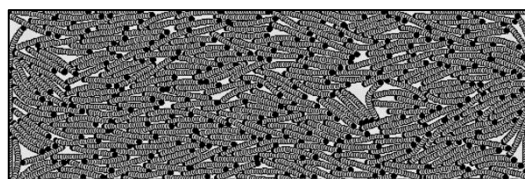
Simulation 2 (acetone)



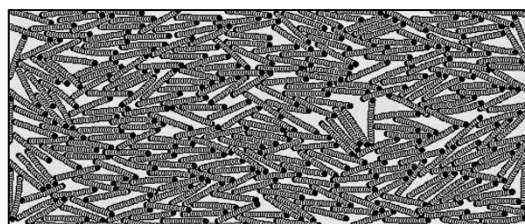
E : $e=3.31$, $\sigma_z=0.26$ kPa



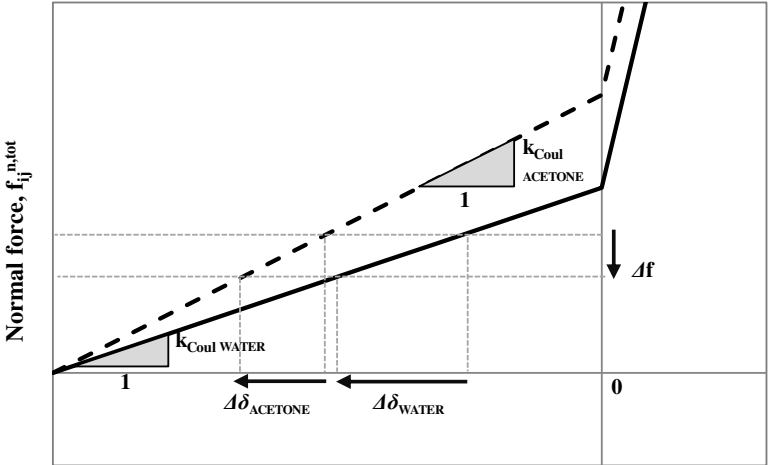
F : $e=1.64$, $\sigma_z=10.00$ kPa



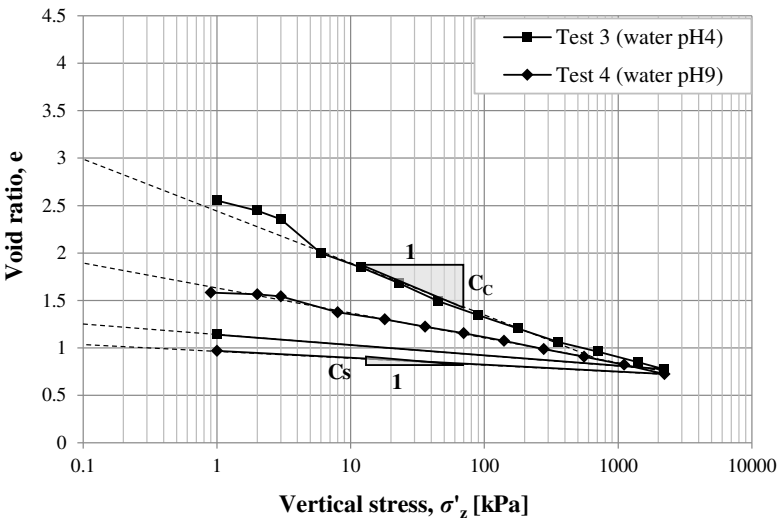
G : $e=0.47$, $\sigma_z=92.3$ kPa

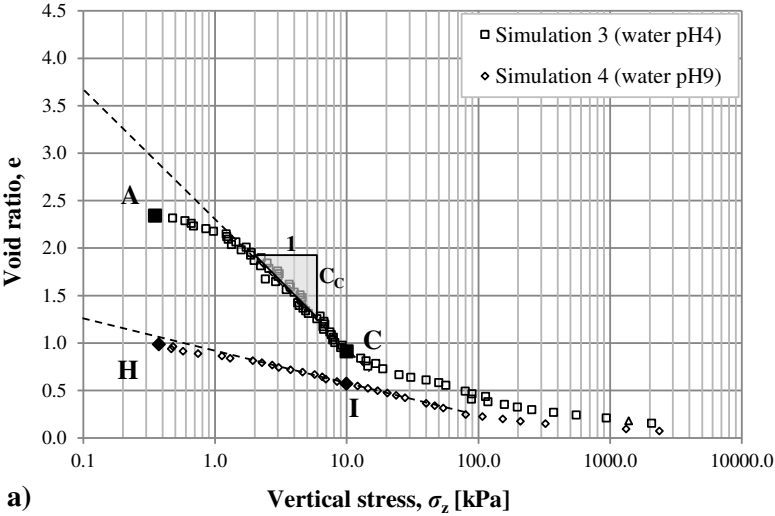


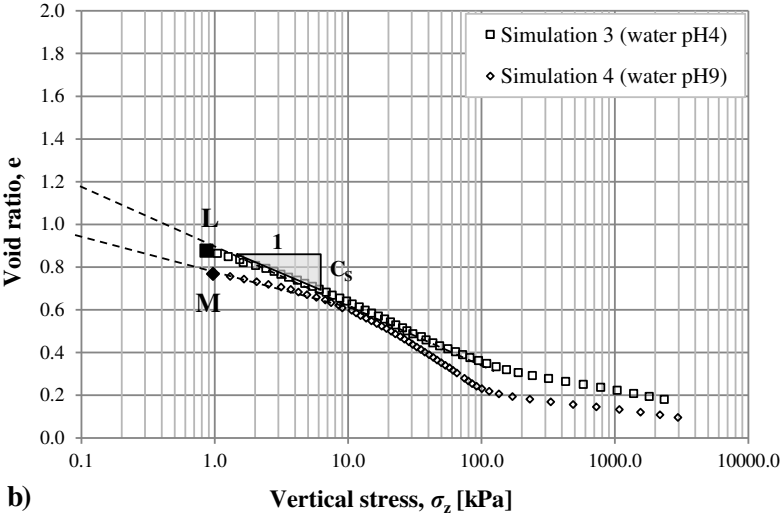
G' : $e=0.85$, $\sigma_z=3.27$ kPa

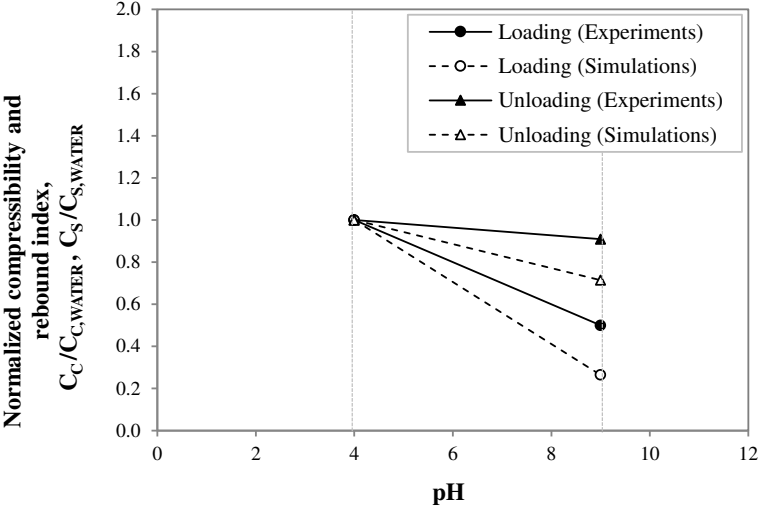


Overlap, δ_{ij}^n					
4	6	4	20	26	24
5	6	4	25	31	29
6	6	4	30	36	34
7	6	4	35	41	39
8	6	4	40	46	44
9	6	4	45	51	49
10	6	4	50	56	54
11	6	4	55	61	59
12	6	4	60	66	64
13	6	4	65	71	69
14	6	4	70	76	74
15	6	4	75	81	79



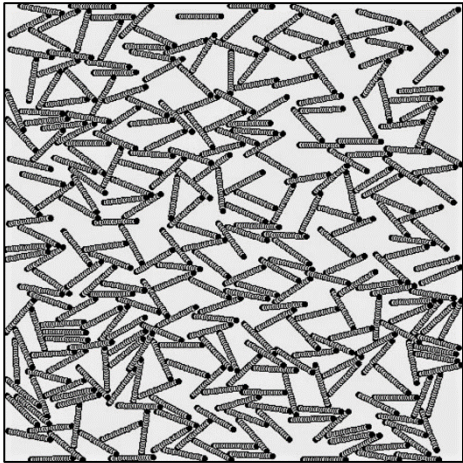




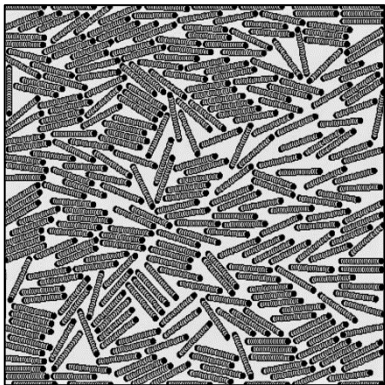


Simulation 3 (water pH4)

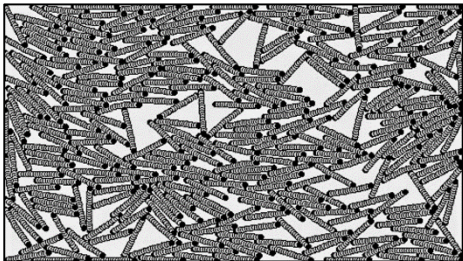
Simulation 4 (water pH9)



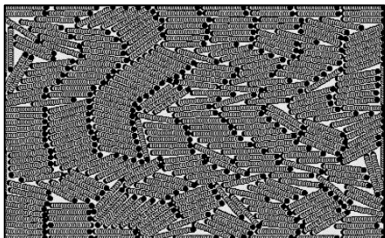
A : $e=2.34$, $\sigma_z=0.35$ kPa



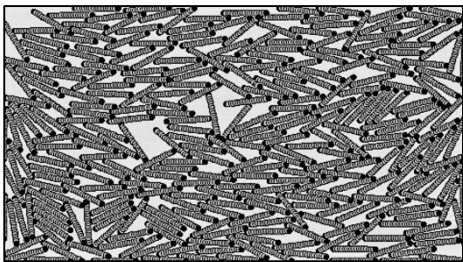
H : $e=0.99$, $\sigma_z=0.38$ kPa



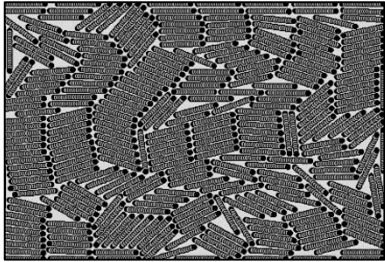
C : $e=0.91$, $\sigma_z=10.01$ kPa



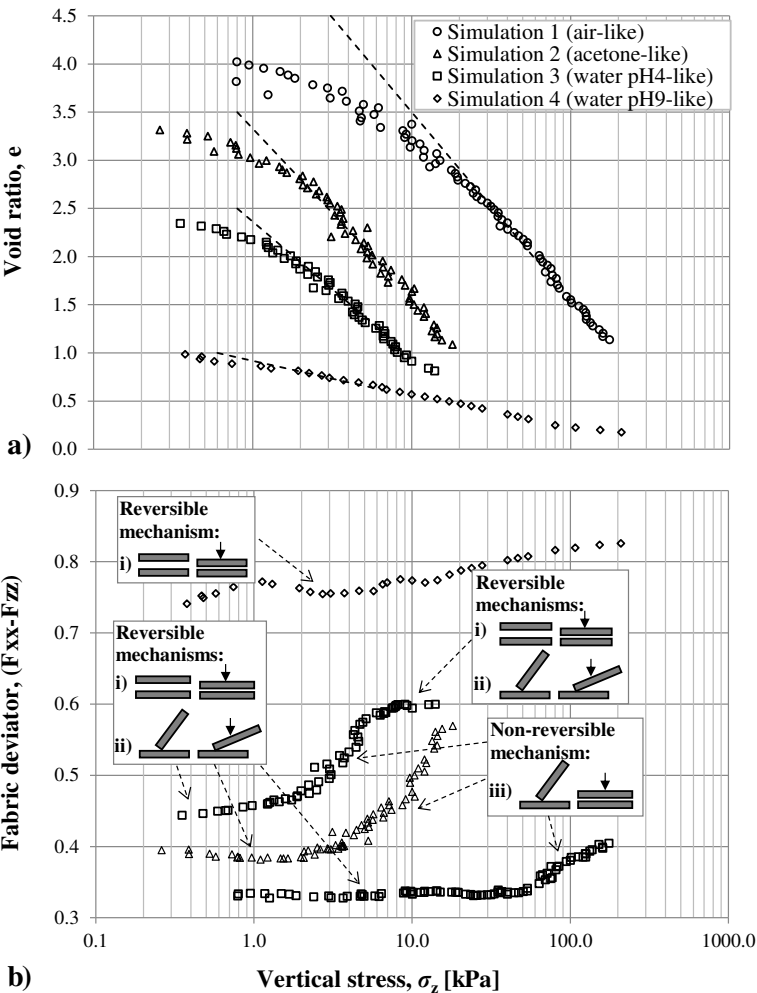
I : $e=0.57$, $\sigma_z=9.97$ kPa

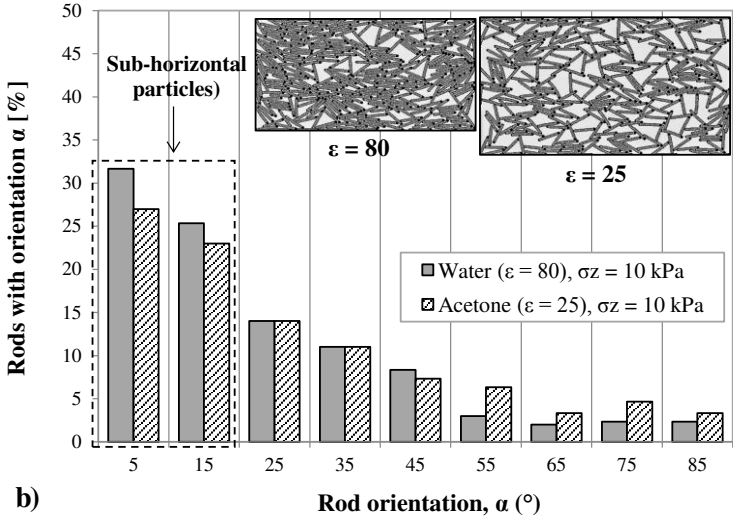
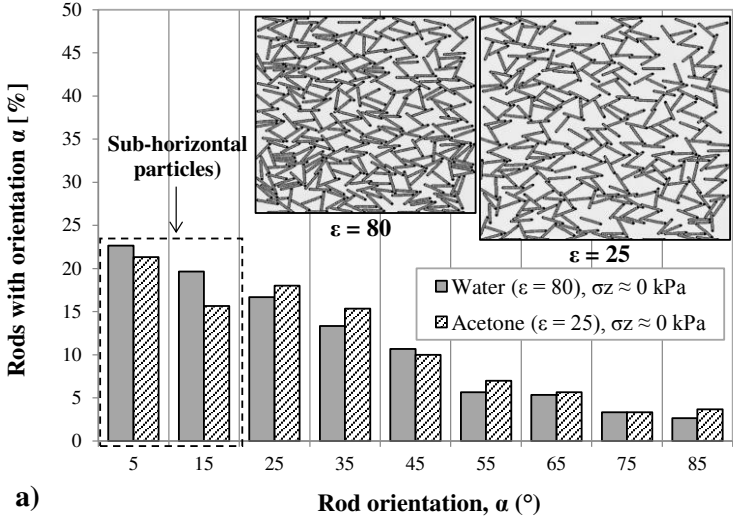


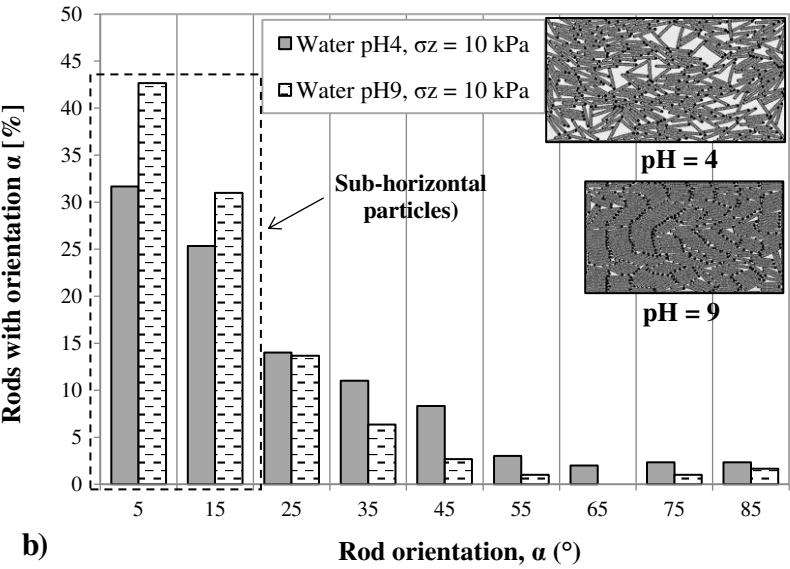
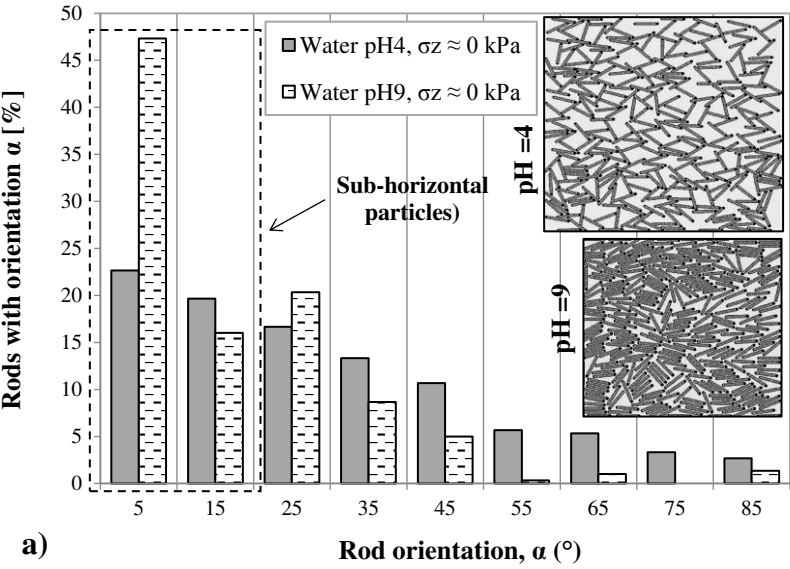
L : $e=0.88$, $\sigma_z=0.87$ kPa



M : $e=0.77$, $\sigma_z=0.97$ kPa







INPUT PARAMETER		VALUE (SI units)
Sphere density	D	2605 kg/m ³
Sphere radius	R	0.5e-6 m
Spheres per rod	N_{s,rod}	19
Number of spheres	N_s	5700
Number of rods	N_{rods}	300
Bonding overlap	δ_{bond}	0.5e-6 m
Threshold overlap	δ_{ij}^{n,*}	0.5e-6 m
Normal stiffness	k_n	1e3 N/m
Tangential stiffness	k_t	2/7k _n
Rolling stiffness	k_{ro}	2/5k _n
Friction	μ	0.3
Normal damping coefficient	γ_n	5.7e-8 kg/s
Tangential damping coefficient	γ_t	2/7γ _n
Rolling damping coefficient	γ_{ro}	2/5γ _n
Background dissipation (relaxation)	Γ_{rel}	3.16e-9 kg/s
Background dissipation (compression)	Γ	3.16e-10 kg/s

Table 1. Properties of the elementary spheres.

	Pore fluid	Dielectric permittivity		pH		Coulombian stiffness [N/m]		Edge charge	Face charge
TEST 1	Air (dry powder)	ϵ^{AIR}	1	-	SIMULATION 1	$k_{\text{Coul}}^{\text{AIR}}$	40	+	-
TEST 2	Acetone	$\epsilon^{\text{ACETONE}}$	25	-	SIMULATION 2	$k_{\text{Coul}}^{\text{ACETONE}}$	1.6	+	-
TEST 3	Water	ϵ^{WATER}	80	4	SIMULATION 3	$k_{\text{Coul}}^{\text{WATER}}$	0.5	+	-
TEST 4	Alkaline water			9	SIMULATION 4			-	-

Table 2. Association between experimental tests and numerical simulations.